Effects of fiber material in concrete manufactured with Electric Arc Furnace Slag: experimental and numerical study

Aratz Garcia-Llona[a,*], Vanesa Ortega-Lopez[b], Ignacio Piñero[c], Amaia Santamaría[d], Miquel Aguirre[e, *]

[a] Centro Tecnológico de Componentes, Calle Isabel Torres 1, 39011 Santander, Spain

[b] Department of Civil Engineering, University of Burgos, Escuela Politécnica Superior, Calle Villadiego s/n, 09001 Burgos, Spain

[c] Tecnalia, Basque Research and Technology Alliance (BRTA), Astondo Bidea, Edificio 700, 48160 Derio, Spain

[d] Department of Mechanical Engineering, University of the Basque Country (UPV/EHU), Escuela de Ingeniería de Bilbao, I (bloque B), Plaza Ingeniero Torres Quevedo, 1, 48013 Bilbao, Spain

[e] Mines Saint-Etienne, Univ Lyon, Univ Jean Monnet, Etablissement Français du Sang, INSERM, U 1059 Sainbiose, F-42023 Saint-Etienne, France

---

Abstract

Over recent years, Electric Arc Furnace Slag (EAFS), a by-product of the steel-making industry, has been used as a replacement of natural aggregates to produce high-performance concrete. In EAFS concrete, fibers are normally added to improve post-cracking behavior, thereby prolonging the durability and range of applications of the composite. Despite the rise in its production, the mechanical performance of fiber-reinforced EAFS concrete is still poorly understood, posing important barriers to its daily use.

This paper aims to study the effect of fiber materials (steel and synthetic) on EAFS concrete performance. To do so, the paper proposes, firstly, an

* Corresponding author:
Email addresses: agarcia@centrotecnologico.com (Aratz Garcia-Llona), miquel.aguirre@emse.fr (Miquel Aguirre).

Preprint submitted to Construction and Building Materials *November 8, 2021*

experimental campaign and, secondly, a numerical simulation to model the effect of fibers both in the pre-cracking and post-cracking stages. Importantly, for the numerical study, an in-house Finite Element (FE) code is developed using interface elements to capture crack propagation. The FE code uses, as input, data obtained in the experimental campaign and is validated against previously unseen experimental results. The overall framework gives important insights on how fibers improve the post-cracking behavior of EAFS concrete and the relevance of fiber material in the overall performance. The validated numerical tool can be used in the future to design EAFS fiber-reinforced concrete structures and therefore increase the applicability of such composite material.

Keywords: *Electric Arc Furnace Slag, Steel/Synthetic fibers, Dog-bone test, Interface solid finite elements, Tensile damage models.*

---

1. Introduction

Concrete is one of the most widely manufactured materials across the world and the expansion of the concrete industry continues apace. It is reported that annual concrete production worldwide increased from more than 10 Gt in 2006 [1] to 32 Gt in 2017 [2]. Set alongside the climate emergency context [3] there is a pressing need to improve the sustainability of concrete production. If that objective is to be fulfilled, then energy-saving techniques, lengthier service lives, and reusability/recycling of materials are among the factors that must therefore be given serious consideration.

In this context, many researchers [4–12] have studied the use of Electric Arc Furnace Slags (EAFS), an industrial waste generated during the steelmaking process, in the replacement of natural aggregates. Reusing EAFS reduces the amounts of waste buried in landfills, while improving certain features of the concrete [12–16].

In a positive sense, EAFS concrete shows a better mechanical performance than other traditional concretes [10,12,16,17]. EAFS high porosity and roughness provides a strong interlocking effect between aggregate and matrix [5,6,12,13,15]. Additionally, the greater durability of EAFS concrete has therefore extended its structural service life [10,13,14]. In a negative sense, the specific density of EAFS is about 15 % higher than natural aggregates, due to metallic inclusions within the slags [18]. Although advantageous for some applications where weight is a key factor (sea-walls, foundations, ballast, etc.), its use is a downside to get self-compacting condition [11,19,20]. Engineers have to take account of the weaknesses of EAFS concrete, just as they have to do for concrete made with natural aggregates, such as brittleness, poor tensile strength, poor resistance to impact strength, fatigue, and low ductility [21]. Previous studies [17,22–24] have proven that additions of randomly distributed small fibers help to address some of these weaknesses. The main role of fibers is essentially to delay crack propagation across the matrix by bridging the crack tips [23,25,26]. However, fiber additions provoke certain problems for mixing and workability. Fibers can show a tendency to clump together, forming balls, or to distribute themselves in non-uniform ways, thereby altering the properties of the composite [14,27,28]. These effects, together with the irregular sizes and shapes of EAFS, makes fiber-reinforced EAFS concrete a heterogeneous material with large inter-sample variability. Its overall reliability is therefore affected, presenting significant obstacles to its widespread adoption for structural purposes [29].

There is therefore a pressing need for a better understanding of the mechanical behavior of EAFS fiber-reinforced concrete. This area has been explored by several authors [14,17,18,29–31], including our recent contributions in [32,33], where it was found that bending strength and post-cracking behavior were improved through the use of EAFS in replacement of natural aggregates and the addition of fibers. Even though very useful insight into the mechanical behavior of the material has been gained from experimental studies, the results are always limited to a specific set of measurements and involve significant time and economic constraints. Limitations that become all the more apparent when large structural components are involved. Computational modeling, and specifically FEA can contribute very accurate quantitative information, such as displacement, stress, and fracture. Additionally, once properly developed and validated, FEA can act as a predictive tool which can be used for the design of structural elements

As far as the authors are aware, no FEA model has been provided for EAFS fiber-reinforced concrete elements and synthetic fiber-reinforced concrete. Building upon our recent experimental contributions [18,32,33], this paper aims to provide an experimental and computational framework to develop an accurate FEA model of EAFS fiber-reinforced concrete including fracture effects. The framework that the authors of this paper have developed not only comprises an accurate finite element model of EAFS fiber-reinforced concrete deformation and fracture, but also a detailed experimental campaign, on small samples, to gather all the necessary model input data. The developed in-house FEM is based on elements with high aspect ratio (interface elements) where tensile damage models are implemented, to describe the behavior of the composite. Interface elements and tensile damage models are capable of capturing concrete fracture and fiber bridging effects, due to steel fiber additions, as also shown in previous research [25,34,35]. In this investigation, the performance of interface elements for modeling synthetic fibers was also analyzed and the numerical framework was validated against the experimental data.

The paper will therefore be organized as follows. Section 2 introduces the numerical and experimental framework giving a brief overview of the tested material, experiments and FEA. In Section 3, the experimental results will be presented and the mechanical performance of steel/synthetic fibers will be assessed. In Section 4, the numerical results will be reviewed and, finally, some concluding remarks will be given in Section 5.

2. Experimental and numerical framework

2.1. Materials

In this research three different mixes are analyzed, in order to study the effects of steel and synthetic fibers on EAFS concrete. The mixes were labeled following the presented nomenclature in [16,32] as: IISC (plain concrete), IISCM (steel fibers) and IISC-Y (synthetic fibers).

The major difference between them concerns the addition of fibers, as is shown in Table 1. Type II cement was used in every mix and high-range water reducing admixture (superplasticizer) was also employed to improve workability and mechanical properties. Not all admixtures are compatible with every cement or fine aggregate and they can cause flowability problems, anomalous rheological behavior or just, not achieving the desired properties [36]. Its compatibility was previously studied in [16].

EAFS were added in two different grading, 4-12 mm and < 4 mm with a fineness modulus of 5.7 and 3.9, respectively. In the absence of fine aggregate (<1.2 mm) due to high energy required to crush EAFS, limestone (95 % of calcite) with a fineness modulus of 1.5 were added to increase the cohesiveness of the paste [16,37]. This grading enabled to achieve the required characteristic in terms of self-compactness and strength. The EAFS were previously subjected to an aging process that consists of irrigating and moving the slag in order to provoke the hydration and carbonation reactions of the possible expansive components presented in it. In this way, the slags maintain its volumetric stability for its application in concrete [6]. The stability of EAFS aggregate was verified by ASTM D-4792 test [38], prolonging the prescribed test duration over 90 days; the results ensured slag expansion smaller than 0.5 %. The design strength of concrete was 40 MPa, as good quality mixes for structural elements, employing a moderate content of binder per cubic meter of concrete.

Table 1: Concrete mix proportions (Kg/m^3)

Constituents	**IISC**	**IISC-M**	**IISC-Y**
CEM II/B-S 42.5R	330	330	330
Admixture	5.3	5.3	5.3
EAFS: $\phi = 4 - 12\ mm$	750	750	750
EAFS: $\phi < 4\ mm$	550	550	550
Limestone: $\phi < 1.2\ mm$	950	950	950
Water	170	180	185
Steel fibers	-	40	-
Synthetic fibers	-	-	4.5

In this study fibers were also added (0.5 % of total volume) in two mixes (IISC-M and IISC-Y) to improve mainly the post-cracking expertise. Two types of fibers were used to improve the performance i) Hooked-end steel fibers (IISC-M) ii) Dimpled-surface synthetic (polyolefin) fibers (IISC-Y). The fact that the designed mixes are self-compacting (absence of vibration) enables not to influence in fiber distribution and direction, which ensures a fairly uniform fiber distribution.

Extensive analyses of these sorts of mixes may be found in previous works [16,18,32,33].

2.2. Experiments

The mechanical properties of the mixes were defined through compression, three-point bending, and tensile tests. The test results are used to define the required inputs by the numerical model and to validate the proposed framework. The properties defined by the proposed set of experiments were:

- Compression test: Compression strength (f_c), compression elastic modulus (E_c) and the Poisson's ratio (ν).
- Three-point bending test: The CMOD/Load curve of sample IISC was used to compute the fracture energy (G_F) and the results of IISC-M and IISC-Y were used to validate the framework of tests that has been proposed.
- Tensile test: Direct tensile strength (f_{td}) and indirect tensile strength (f_{ti}).

Compression and bending tests are well-known and they were performed according to the specifications described in the European standards [39–41]. However, tensile strength is not a frequently defined property for concrete. It can either be determined by an indirect tensile test (Brazilian test) or a direct tension test (Dog-bone test) [42–45].

The Brazilian test (or splitting tensile test) is a well-known method for determining tensile strength through compressive loading. It was performed in accordance with UNE-EN 12390-6 [46].

Direct tensile tests are hardly used for concrete and there are insufficient standards or instructions on the performance of these tests [45]. In this research, the direct tension test was performed using small size Dog-bone shaped specimens subjected to direct monotonic tensile loading. The dog-bone specimen was designed based on the dimensions proposed in [45]. The overall length of the specimen is 164.1 mm and the cross-section at the head of the specimen was 55.5 x 30 mm, as shown in Figure 1. These dimensions, together with the clamping jaws, mean that the specimen can be easily aligned with no undesired rotations or constraints. These features are useful for capturing uniaxial tensile behavior in the narrow section. Lastly, the Dog-bone molds with the above measurements were built using a 3D printer.

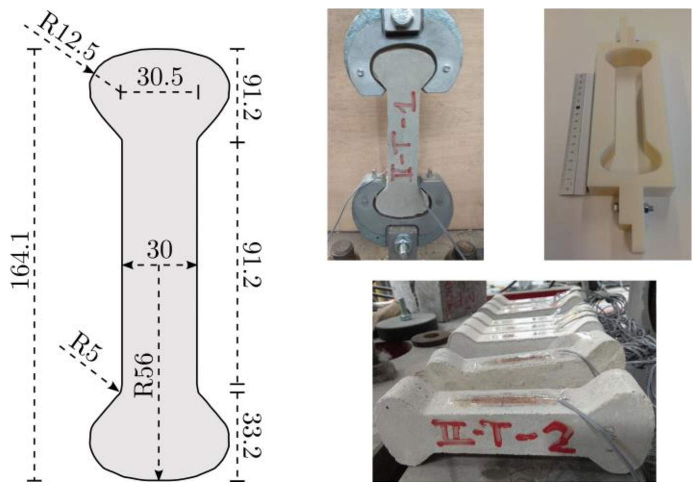

Figure 1 Dog-bone test set up (mm)

2.3. Finite Element Analysis: Interface elements

Discontinuities are generated in solids when they are loaded beyond their elastic limits. From a mechanical point of view, they can be modeled as weak 145 or strong discontinuities. A weak discontinuity is characterized by a continuous displacement field and discontinuous strain. In contrast, the strong discontinuity kinematics is characterized by unbounded strain field along the discontinuity surface. The modeling of strong discontinuities is common in elements with irregular displacement fields and highly localized failures [47] such as in brittle materials (EAFS concrete).

A technique based on the insertion of interface elements with a high aspect ratio between regular elements of the mesh is used to describe the kinematics associated with the discontinuities [34,45]. In this method, a solid is therefore idealized as a two phase -interface elements and bulk elements- composite, as illustrated in Figure 2. Bulk elements are considered elastic elements and interface element behavior is governed by a softening law, which models concrete fracture or bridging phenomena. Crack openings are simulated by the degradation of interface elements. The governing equation in linear elasticity (weak form) provides an approximate solution to the structural mechanics of the composite:

$$-\mathbf{W}\cdot\int_{\Gamma} \boldsymbol{\sigma}\mathbf{n}\,\mathrm{d}\Gamma + \int_{\Omega} \boldsymbol{\sigma}:\nabla\mathbf{W}\,\mathrm{d}\Omega = \mathbf{W}\cdot\int_{\Omega} \boldsymbol{f_b}\,d\Omega \tag{1}$$

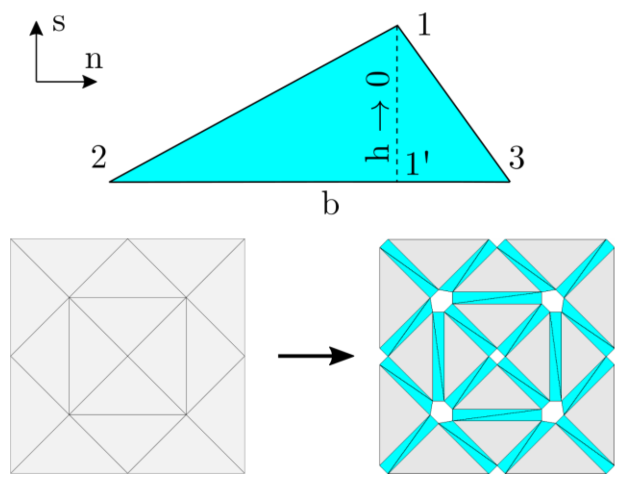

Figure 2: 2D Interface element

where, **W** is the weight function, $\boldsymbol{\sigma}$ is the stress field, **n** is the normal vector, Γ is the boundary, Ω is the surface of the solid and $\boldsymbol{f_b}$ are the body forces.

The triangular element is geometrically defined by the nodal coordinates, which are used to calculate the normal vector, **n**, to the base, b, and the height of the element, h, as shown in Figure 2. Once the geometry is defined, the strain tensor (ϵ) can be written as the summation of the components of the strain tensor that depend on h ($\hat{\epsilon}$) and on b of the triangle ($\tilde{\epsilon}$):

$$\epsilon = \tilde{\epsilon} + \hat{\epsilon} = \frac{1}{b}\begin{bmatrix} 0 & \frac{1}{2}\left(u_n^{(3)} - u_n^{(2)}\right) \\ \frac{1}{2}\left(u_n^{(3)} - u_n^{(2)}\right) & u_s^{(3)} - u_s^{(2)} \end{bmatrix} + \frac{1}{h}\begin{bmatrix} [\![u]\!]_n & \frac{1}{2}[\![u]\!]_s \\ \frac{1}{2}[\![u]\!]_s & 0 \end{bmatrix} \tag{2}$$

where, $u_n^{(i)}$ and $u_s^{(i)}$ are the normal and tangential displacements and $[\![u]\!]_n$ and $[\![u]\!]_s$ are the relative displacements of node 1 and its projection onto the base, 1'.

Interface elements can be of either zero thickness or very little height ($h \to 0$). This condition indicates that $\tilde{\epsilon}$ tends to be infinite (unbounded), as might be deduced in Equation 2. Therefore, the strains are almost dependent on $\tilde{\epsilon}$. The kinematics of the solution is conditioned mainly by the relative displacements between node 1 and its projection 1', h [34,35].

Then, the corresponding stresses can be calculated by the constitutive models, even though the strain tensor is unbounded. The tension damage model used to describe the behavior of interface elements is as follows:

$$\boldsymbol{\sigma} = (1 - \mathrm{d})\,\mathbb{C} : \boldsymbol{\epsilon} = (1 - \mathrm{d})\,\mathbb{C} : (\tilde{\boldsymbol{\epsilon}} + \hat{\boldsymbol{\epsilon}}) \approx (1 - \mathrm{d})\,\mathbb{C} : \hat{\boldsymbol{\epsilon}} = \frac{1 - \mathrm{d}}{\mathrm{h}}\mathbb{C} : (\mathbf{n} \otimes [\![\mathbf{u}]\!])^{\mathrm{s}} \tag{3}$$

where, d is the damage parameter, $\mathbb{C}$ is the elastic tensor, and $(\ )^s$ refers to the symmetric part. The damage criterion, ϕ, is defined in terms of equivalent stress, $\tilde{\sigma}$, and a stress-like internal variable q(r):

$$\phi = \tilde{\sigma} - q(r) \leq 0 \tag{4}$$

The equivalent stress is computed through the stresses at the base of the triangle while q(r) synthesizes the softening behavior of the composite. The adopted bridging law is used to represent traction-separation laws for different steel-fiber-reinforced concrete in [25]:

$$q(r) = \left(f_{t,com} - t_1\right) e^{\frac{-r}{\omega_{ref}}} + t_1 \frac{\omega_u - r}{\omega_u} + t_2\, r\, e^{c_1 - c_{2r}} \tag{5}$$

where, r is a strain-like internal variable, $f_{t,com}$ is the tensile strength of the composite, t_1, t_2, c_1, and c_2 are the fitting coefficients, ω_{ref} is the reference crack opening displacement, and ω_u is the ultimate crack opening. $f_{t,com}$ is derived from the tensile tests. In contrast, ω_{ref} is determined through fracture energy, (G_F), calculated from the three-point bending test applied to plain concrete (IISC).

$$\omega_{ref} = \frac{f_t}{G_F} \tag{6}$$

The first term of Equation 5 is associated with the fracture of plain concrete. The second term introduces the frictional aspect during the pullout procedure. The last term is correlated with the anchorage effect that some fibers might have due to their shape, such as the hooked-end fibers.

3. Experimental test results and discussion

The properties defined through the proposed tests are listed in Table 2 (mean values and the standard deviation in parentheses). The addition of steel fibers has hardly any effect on the compressive strength, as other authors have also concluded [17,32,48]. The tensile elastic modulus tended to be slightly higher than the compressive elastic modulus for the mix with fibers, as also found in previous studies [49]. The Dog-bone test provides lower tensile stress than the Brazilian test as previous studies suggested [50]. The values of uniaxial tensile strength were 17 %, 22 % and 16 % lower than the indirect tensile strength for IISC, IISC-M and IISC-Y mixtures, respectively.

Table 2: Compressive, tensile and three-point bending test results.

Property	**IISC**	**IISC-M**	**IISC-Y**
f_c **(MPa)**	59.66 (5.7)	53.09 (1.5)	46.08 (1.0)
E_c **(GPa)**	40.1 (0.7)	34.7 (1.5)	31.6 (0.9)
ν	0.23	0.22	0.22
f_{td} **(MPa)**	4.25 (0.2)	3.77 (0.4)	3.66 (0.4)
f_{ti} **(MPa)**	5.11 (0.5)	4.84 (0.6)	4.35 (0.4)
E_t **(GPa)**	38.5 (1.0)	37.9 (2.8)	35.5 (0.3)
G_F **(N/mm)**	0.137	2.235	0.598

Figure 3 shows the stress-strain curve of the Dog-bone test of the three mixes. The samples were preloaded in 6 cycles of loading/unloading which enables to assess the hysteric behavior of the mixes. In Figure 3(a) is more evident that the slope of the loading/unloading curves is reduced which means the material is damaged and the stiffness is reduced. Mixes with fibers (IISC-M and IISC-Y) exhibit an improved hysteretic response in terms of stiffness which increase the energy absorbing capacity. Despite possible size-effect uncertainties [51,52], these results are aligned with the expected tensile behavior [49,50]. Although more tests are still required to provide more certain conclusions, it is an indicator of the potential of the addition of fibers.

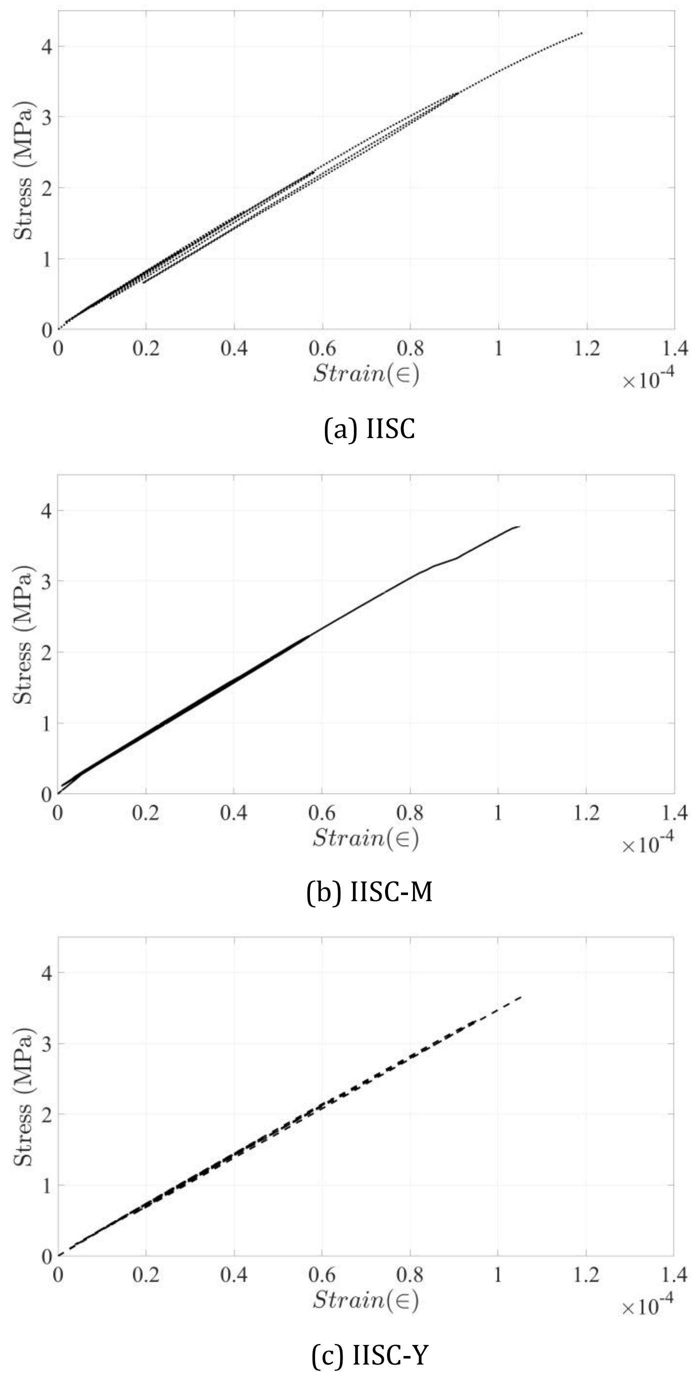

Figure 3: Strain-stress curve of Dog-bone test.

The tensile strength of concrete is usually defined through empirical relations based on compressive strength. In Figure 4, empirical curves for plain concrete suggested by International Federation for Structural Concrete (CEB-FIB) [53] and American Concrete Institute (ACI-318) [54] are drawn together with the empirical equation proposed for fiber-reinforced concrete by *Xu et al.* [55]. All the mixes are consistent with the proposed equations with ratios ranging between 7-12 %. Tensile strength is often approximated as a tenth of compressive strength [56], which is also applicable in fiber-reinforced EAFS concrete.

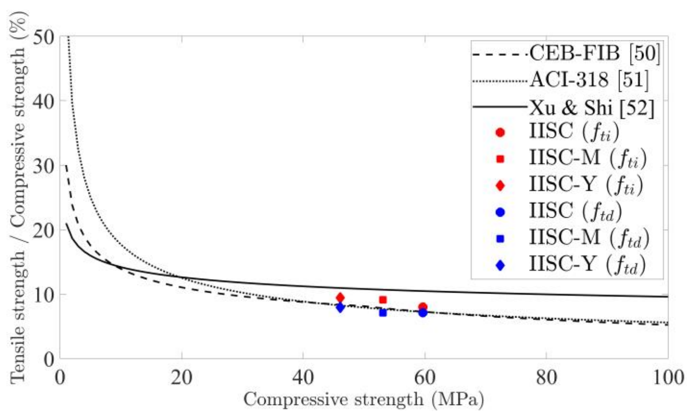

Figure 4: Relationship between tensile strength and compressive strength.

Figure 5 illustrates the CMOD/load curves defined in the three-point beam tests, in accordance with [41]. The cross-sectional dimensions of the notched beams were 150 mm by 150 mm, each with a length of 600 mm and a span of 550 mm. The notch was marked to a depth of 25 mm at mid span on the bottom side of each beam.

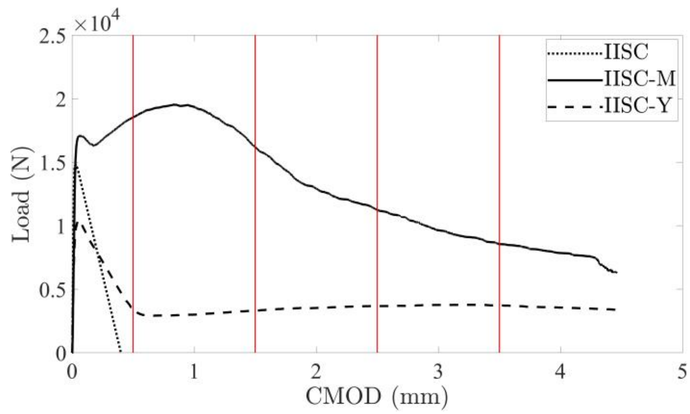

Figure 5: Average CMOD/Load curves of the notched beam test.

Fracture energy (G_F) is a parameter used to model the post-cracking behavior of concrete. It is computed with the model proposed by *Hilleborg* [57], using the load/CMOD curve. Fracture energy dissipated up to a CMOD of 3.5 mm is reported in Table 2. From a design point of view, it is assumed that no further energy could have been absorbed after that point [26].

Figure 5 shows the load/CMOD curves of IISC, IISC-M, and IISC-Y. Focusing on the pre-fracture behavior (damage stage), IISC-M shows slightly greater values of load than IISC in line with the behavior reported in the tensile tests. IISC-Y shows slightly greater values of load than IISC, in line with the behavior reported in the tensile tests. IISC-Y shows lower values than plain concrete that is consistent with the worst mechanical performance shown in Table 2. This last difference might be due to factors relating to the manufacturing process that increased the air content of the mixes [22] and the lower stiffness of the synthetic fibers [17,22,58].

Beyond the first peak, the fibers play an increasingly prominent role and their effects become more evident, mainly depending on the dosage and properties of the fibers [23,59]. IISC showed a brittle behavior, while the fiber mixes maintained some residual strength after the crack, so their behavior was more ductile than the former. Three notched beams were tested for IISC-M and IISC-Y. IISC-Y samples showed very similar behavior while IISC-M presented higher variability between the samples (see Figure 8). This variation is related with the uncertainties introduced when fibers are added to the mix [59]. The improvement in the post-cracking behavior of IISC-M became particularly relevant, multiplying by 3-6 the residual strength of mix IISC-Y.

4. Finite Element Analysis

The notched beams (IISC-M and IISC-Y) are numerically analyzed in this section, using the Finite Element algorithm described in section 2.3. To do so, the FE model of the notched beam is firstly defined in section 4.1. Secondly, the numerical model is validated against experimental data in section 4.2. Finally, in section 4.3, the validated model is used to extract physical quantities that allow improving the insight into the fracture mechanics of the fiber-reinforced beams. Such physical quantities would otherwise be impossible or too difficult to estimate from experimental measurements.

4.1. Definition of the Finite Element Model

Figure 6 illustrates the finite element model and the boundary conditions of the notched beams presented in Section 3. The numerical analysis is carried out in 2D and plane stress conditions are considered. An unstructured mesh is used to reduce the dependency of the cracking path with the mesh. It is meshed with linear triangular elements of 10 mm. The mesh is refined (1 mm) near the notch where the crack is expected to develop, to capture the cracking more accurately. Table 3 lists the material properties of the bulk elements defined through the tests while interface elements (0.001 mm) properties are reported in Table 4. Interface elements inputs are defined by fibers properties except for Poisson’s ratio, which is assumed as null to introduce the discrete relation between nodes based on Young’s modulus [35].

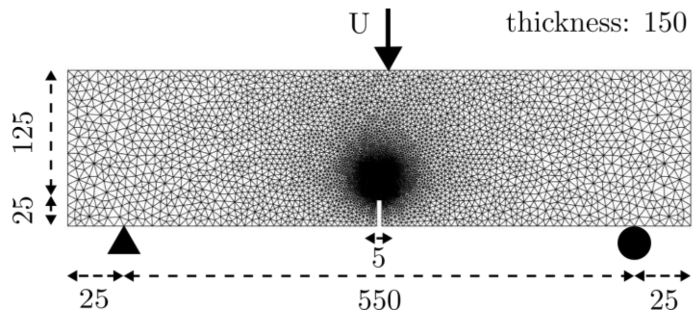

Figure 6: Finite element model of notched test beams (mm).

Table 3: Material parameters used to model Bulk elements.

INPUT	**IISC-M**	**IISC-Y**
Compressive strength, f_c (MPa)	53.09	46.08
Young's modulus, E_c (MPa)	34.7×10^3	31.6×10^3
Poisson's ratio, ν	0.22	0.22
Direct tensile strength, f_{td} (MPa)	3.77	3.66
Indirect tensile strength, f_{ti} (MPa)	4.84	4.35
Fracture energy, G_F (N/mm)	0.137	0.137

The used numerical model is very sensitive to the length of the loading steps. Figure 7 shows the load/CMOD curve of the IISC-Y beam modeled with three displacement steps (10^{-2}, 10^{-3} and 10^{-4} mm). The improvement is significant while the loading step decreased, especially at the maximum loading point. The post-cracking part is almost the same for the three settings. A loading step of 10^{-4} mm is set for the three mixes, seeking a balance between accuracy and computational cost.

Table 4: Material parameters used to model Interface elements

INPUT	IISC-M	IISC-Y
Young's modulus (MPa)	210×10^3	6×10^3
Poisson's ratio	0	0
Tensile strength (MPa)	1,200	400
Fiber length/diameter (mm/mm^2)	35/0.55	35/0.93
Fiber volume content (%)	0.5	0.5
Fiber shape	Hooked-end	Dimpled-surface

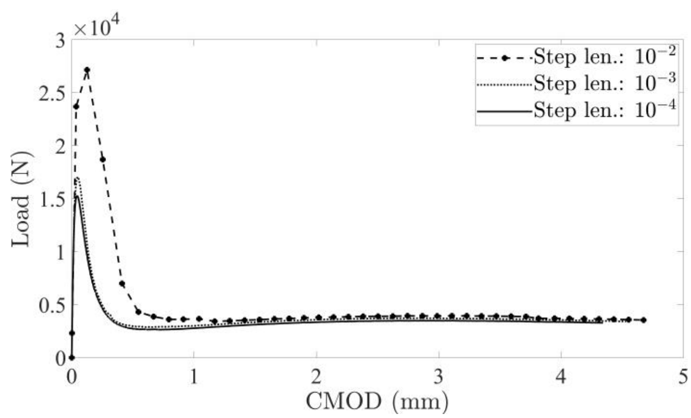

Figure 7: Comparison of IISC-Y notched beams modeled with different pseudo-step length.

4.2. Validation of the Finite Element Model

The structural responses of the three samples are presented in Figure 8 in terms of load/CMOD. The numerical results are computed with the tensile strength from both the Dog-bone test (f_{td}) and the Brazilian test (f_{ti}) as inputs.

The numerical curves are in good agreement with the experimental ones in both tests, although there are slight differences between them.

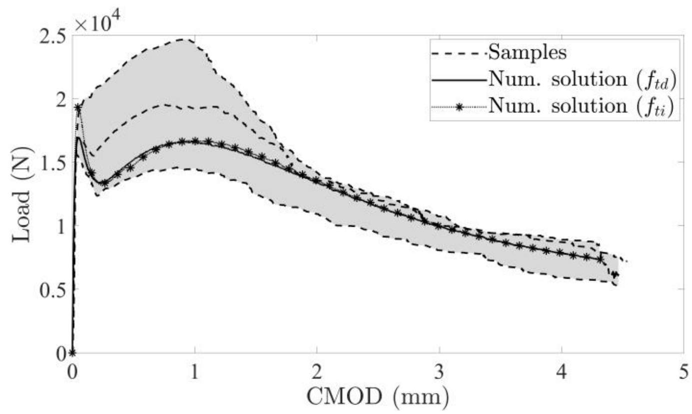

(a) IISC-M

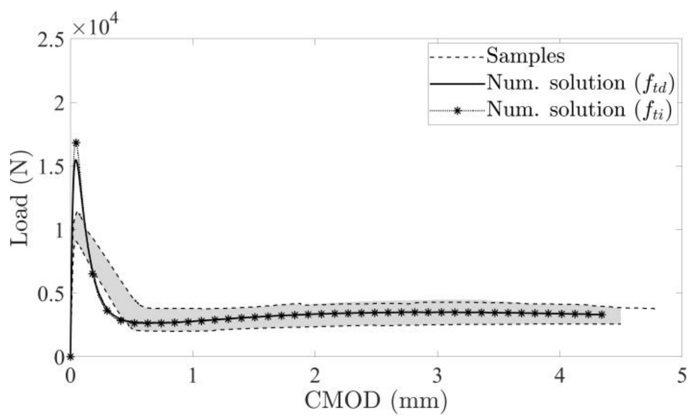

(1) IISC-Y

Figure 8: CMOD/load curve of IISC-M and IISC-Y notched beams.

Focusing on the first stage (pre-cracking) of the curves, the mechanical behavior is mainly described by the tensile strength and the elastic parameters of the mixes. It is evident that the curves that are modeled using f_{td} shows a better fit than the models that are defined using f_{ti}. At the peak, the difference of the curves modeled with f_{td} and f_{ti} compared to the experimental curve for IISC-M is 0.5 % and 13.5 %, respectively, while for IISC-Y is 45 % and 63 %. One explanation is that the interface elements are only damaged by normal stresses at the base of the interface element and not by shear stresses. The Dog-bone test represents this fracture mode (Mode I) better than the Brazilian test. Even though the Brazilian test is standardized and commonly used to define tensile strength, the results confirmed that the Dog-bone test provides more suitable inputs.

The post-cracking stage mainly depends on the fiber properties and quantity (bridging phenomena). The parameters of the bridging law presented in Equation 5 are defined as $t_1 = 0.6$, $t_2 = 1.45$, $c_1 = 1.7$, and $c_2 = 2.0$ for IISC-M and as $t_1 = 0.1$, $t_2 = 0.2$, $c_1 = 1.0$, and $c_2 = 0.6$ for IISC-Y. In Figure 8(a), IISCM shows a hardening behavior in its post-cracking behavior while mix IISC-Y shows a softening behavior, due to the fiber material difference. After the first peak in IICS-M, there is a decline, reflecting the inactivity of the steel fibers in response to concrete cracking. Then, the steel fibers are activated and the better anchoring conditions meant that the load can be increased after cracking. The improved anchoring effect is a result of the fiber shape (hooked-end fibers) and the high elastic modulus, which increases the pull-out resistance. The numerical solution captures this effect and it remains within the shaded range throughout the post-cracking stage. In Figure 8(b), although the peak of the numerical solution overestimates the peak, the proposed numerical model could also be considered suitable for synthetic fibers.

4.3. Numerical analysis

Once the FEM is validated with the experimental load/CMOD curves, it constitutes an advanced numerical tool that provides quantitative information on every point of the beam at any loading step. It facilitates the analysis of aspects that are difficult to estimate analytically, such as stress field, internal displacements, crack development, damage level, and fiber effectiveness.

Stresses are the responsible for crack formation and the numerical analysis provides the stresses of every element. Figure 9 illustrates the stress concentration points and their evolution during the loading process. Maximum stresses are located at the supports, loading point and the peak of the crack. The crack reduces the load-bearing surface, which increases the stresses throughout the beam and specially at the loading point. Once the crack crosses the beam, the stress along the beam decreases while the CMOD rapidly increases up until failure.

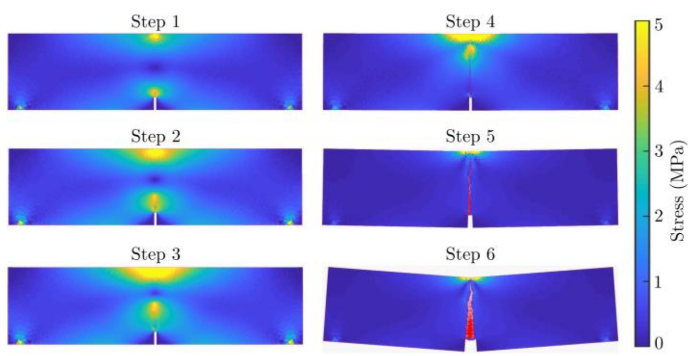

Figure 9: Stress concentration at the peak of the crack (IISC-Y).

As result of increasing stresses, the beam is damaged and cracks starts to develop. The IISC notched beams shows brittle failure (sudden fracture) while the mixes with fibers retained a residual strength, as may be concluded from the tests (Figure 10). Both failure modes, as illustrated in Figure 11, could be described through the interface elements. The load/deflection curves computed through FEM are consistent with the failure modes observed in the experimentation. The IISC beams lose all their strength and the crack crosses the beam at a deflection of 1 mm. Nevertheless, the fibers sew the crack, which means that the reinforced mixes retained a residual strength.

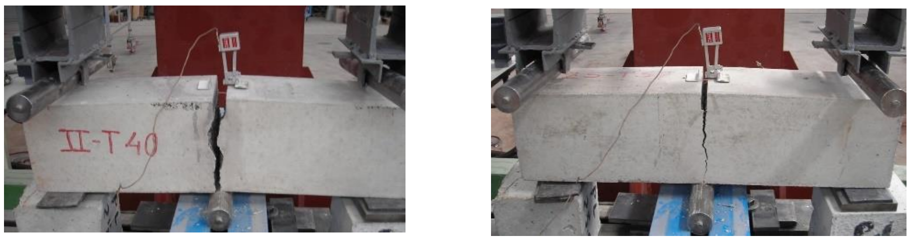

(a) IISC (a) IISC-Y

Figure 10: Fracture mechanics

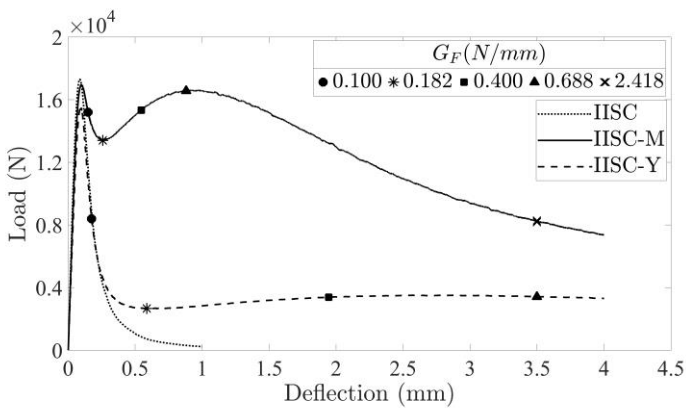

Figure 11: Load/deflection curve defined in FEM

Table 5 presents the numerical results to assess the performance of synthetic and steel fibers at deflections of 0.001, 0.004, 0.2, 1.0, and 3.5 mm. As they are analyzed at the same deflection, damage levels and CMOD are very similar in both mixes. However, there are differences between the computed load and the fracture energy that is applied to arrive at these states. The difference is at times appreciable, especially after the deflection of 0.2 mm. IISC-Y in particular loses most of its strength at a deflection of 1 mm where the energy dissipation rate drops and crack openings begin to increase significantly. At this point, fracture energy also starts to increase, in a way that is consistent with the definition given in [57]. Mixes with steel fibers also replicate this tendency. The computed fracture energy for both cases match the experimental values presented in [32].

Table 5: Cracking development based on deflection (0.001, 0.004, 0.2, 1 and 3.5 mm).

Absolute Damage (%)					
IISC-M	0.02	1.35	8.60	9.25	9.37
IISC-Y	0.01	1.03	9.12	9.35	9.36
CMOD (mm)					
IISC-M	0.003	0.012	0.161	1.006	3.765
IISC-Y	0.003	0.012	0.181	1.072	3.797
Fracture energy (N/mm)					
IISC-M	7×10^{-4}	0.011	0.140	0.794	2.418
IISC-Y	6×10^{-4}	0.001	0.110	0.243	0.688
Load (kN)					
IISC-M	2.2	9.7	13.8	17.2	8.1
IISC-Y	2.2	9.2	6.9	2.9	3.7

Table 6 depicts data to analyze the post-cracking performance according to fracture energy. It is worth noting that fracture energy is related to the crack growth resistance [57]. As the pull-out resistance of a synthetic fiber is lower, damage to IISC-Y appears earlier than in the mix with steel fibers. IISCM requires higher load values and shows a lower CMOD at the same energy levels. This substantial difference reveals the anchoring effect and higher elastic modulus of the steel fibers. The corresponding loading points of the G_F under study are labeled in the load/deflection curves shown in Figure 11, highlighting the effects of added fibers. The fracture energy that is required by IISC-Y is dissipated by IISC-M at a deflection of 0.881 mm, underlining the advantageous effects of steel fibers.

Table 6: Cracking development based on fracture energy (0.1, 0.182, 0.4, 0.688, and 2.418 N/mm).

Damaged interface elements					
IISC-M	1,693	1,785	1,811	1,816	1,831
IISC-Y	1,822	1,861	1,861	1,861	-
Relative damage level (%)					
IISC-M	87.74	93.92	97.46	98.57	100
IISC-Y	95.98	99.90	99.99	100	-
Load (kN)					
IISC-M	15.20	13.40	15.33	16.56	8.23
IISC-Y	8.39	2.66	3.38	3.41	-
CMOD (mm)					
IISC-M	0.104	0.223	0.521	0.877	3.763
IISC-Y	0.147	0.617	2.099	3.795	-

Fracture mechanics may be studied in-depth through the behavior of the interface elements. These are only introduced in the central area where cracks are expected, due to the existence of a weakness (notch). Figure 12 shows crack growth and damage evolution on interface elements at different values of G_F (0.100, 0.182, 0.400, 0.688, and 2.418 N/mm). Damage level starts to be relevant in the mix IISC-M about G_F = 0.001 N/mm. Until then, most of the interface elements are in the elastic domain. G_F = 0.182 N/mm is related to the activation point of the steel fibers while G_F = 0.400 N/mm is an intermediate point of the hardening curve of IISC-M. G_F = 0.688 and 2.418 N/mm are fracture energy values at the failure points of IISC-Y and IISC-M, respectively. The differences between the mixes are visible since the beginning of the post-cracking stage. The crack crosses the IISC-Y beam at G_F of 0.182N/mm whereas the IISC-M beam is at 0.400 N/mm. Another interesting fact is damage distribution, specially at the top part of the beam. Interface elements are slightly damaged, except for the crack in IISC-Y. However, the damage to mix IISC-M is further distributed, showing higher levels of damage in the top part. This fact is further evidence of the greater ductility of the mixes reinforced with steel fibers.

The numerical results of this method confirmed that it is a promising tool for the fracture analysis of EAFS concrete. Not only may it be used for mixes reinforced with steel fibers [34,35], but it can also be used for synthetic fibers. The application of this technique can likewise provide quantitative information related to fracture mechanics that is difficult to determine through experimentation.

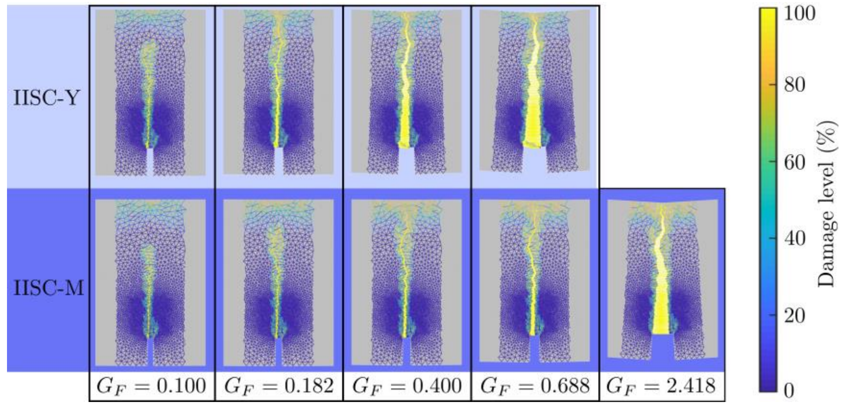

Figure 12: Development of damage level according to fracture energy (N/mm).

5. Conclusions

A framework is presented in this paper for the study of fiber-reinforced EAFS concrete from an experimental and numerical point of view. A set of tests is proposed to define the inputs required by the numerical model, which is validated with notched beams made of fiber-reinforced EAFS concrete.

From a mechanical point of view, fibers influence mainly the tensile behavior (Fracture energy, toughness and residual stress) of the mixes changing the failure mode from brittle behavior to a more ductile behavior. In particular, the positive effect of steel fibers must be reported improving remarkably the postpeak behavior.

The numerical analysis shows that the proposed method is able to model fracture and fiber bridging effects. The tensile strength required by the bridging model is determined through direct and indirect tests. It is concluded that the proposed Dog-bone test provides more suitable values to describe the bridging model implemented on the interface elements.

The numerical framework provides valuable information to understand damage and cracking mechanisms. The numerical results confirms the validity for synthetic fibers and provides further evidence that the interface elements are suitable for modeling the steel-fiber bridging effect.

The framework that has been developed can facilitate deeper understanding of the effects of fibers at a material-scale, through the study of fiber materials, volume, content, and shape. It is also a promising tool to apply to large-scale structures.

Importantly, future research could well investigate the behavior of EAFS concrete in large-scale structures under varied loading conditions. In addition, further research is needed to confirm the good performance of the numerical method at producing accurate descriptions of the fiber bridging effect.

Acknowledgment

The authors wish to express their gratitude to the following entities for having funded this research work: the Spanish Ministries MCI, AEI, EU and ERDF [RTI2018-097079-B-C31; PID2020-113837RB-I00; 10.13039/501100011033]; the Junta de Castilla y León (Regional Government) and ERDF [UIC-231, BU119P17]; the Basque Government research group [IT1619-22 SAREN]; the University of Burgos [Y135.GI]. Likewise, our thanks to CHRYSO and HORMOR for supplying the materials used in this research.

References

[1] C. Meyer, The greening of the concrete industry, Cem. Concr. Compos. 31 (2009) 601–605. https://doi.org/10.1016/j.cemconcomp.2008.12.010.

[2] Arosio V, Arrigoni A, Dotelli G, Reducing water footprint of building sector: concrete with seawater and marine aggregates, in: IOP Conf. Ser. Earth Environ. Sci., 2019. https://doi.org/10.1088/1755-

1315/323/1/012127.

[3] European Parliament, Climate and environment emergency., 2019. https://www.europarl.europa.eu/doceo/document/TA-9-2019-0078_EN.pdf.

[4] S.I. Abu-Eishah, A.S. El-Dieb, M.S. Bedir, Performance of concrete mixtures made with electric arc furnace (EAF) steel slag aggregate produced in the Arabian Gulf region, Constr. Build. Mater. 34 (2012) 249–256. https://doi.org/10.1016/J.CONBUILDMAT.2012.02.012.

[5] Y.R. Alharbi, A.A. Abadel, N. Elsayed, O. Mayhoub, M. Kohail, Mechanical properties of EAFS concrete after subjected to elevated temperature, Ain Shams Eng. J. 12 (2021) 1305–1311. https://doi.org/10.1016/J.ASEJ.2020.10.003.

[6] I. Arribas, A. Santamaría, E. Ruiz, V. Ortega-López, J.M. Manso, Electric arc furnace slag and its use in hydraulic concrete, Constr. Build. Mater. 90 (2015) 68–79. https://doi.org/10.1016/J.CONBUILDMAT.2015.05.003.

[7] J.M. Manso, V. Ortega-López, J.A. Polanco, J. Setién, The use of ladle furnace slag in soil stabilization, Constr. Build. Mater. 40 (2013) 126–134. https://doi.org/10.1016/J.CONBUILDMAT.2012.09.079.

[8] M. Skaf, J.M. Manso, Á. Aragón, J.A. Fuente-Alonso, V. Ortega-López, EAF slag in asphalt mixes: A brief review of its possible re-use, Resour. Conserv. Recycl. 120 (2017) 176–185. https://doi.org/10.1016/J.RESCONREC.2016.12.009.

[9] A. Santamaría, E. Rojí, M. Skaf, I. Marcos, J.J. González, The use of steelmaking slags and fly ash in structural mortars, Constr. Build. Mater. 106 (2016) 364–373. https://doi.org/10.1016/J.CONBUILDMAT.2015.12.121.

[10] P. Tamayo, J. Pacheco, C. Thomas, J. de Brito, J. Rico, Mechanical and Durability Properties of Concrete with Coarse Recycled Aggregate Produced with Electric Arc Furnace Slag Concrete, Appl. Sci. 2020, Vol. 10, Page 216. 10 (2019) 216. https://doi.org/10.3390/APP10010216.

[11] C. Pellegrino, F. Faleschini, Experimental behavior of reinforced concrete beams with electric arc furnace slag as recycled aggregate, ACI Mater. J. 110 (2013) 197–205. https://doi.org/10.14359/51685534.

[12] R. Vaiana, F. Balzano, T. Iuele, V. Gallelli, Microtexture Performance of EAF Slags Used as Aggregate in Asphalt Mixes: A Comparative Study with Surface Properties of Natural Stones, Appl. Sci. 2019, Vol. 9, Page 3197. 9 (2019) 3197. https://doi.org/10.3390/APP9153197.

[13] C. Pellegrino, V. Gaddo, Mechanical and durability characteristics of concrete containing EAF slag as aggregate, Cem. Concr. Compos. 31 (2009) 663–671. https://doi.org/10.1016/J.CEMCONCOMP.2009.05.006.

[14] V. Ortega-López, J.A. Fuente-Alonso, A. Santamaría, J.T. San-José, Á.

Aragón, Durability studies on fiber-reinforced EAF slag concrete for pavements, Constr. Build. Mater. 163 (2018) 471–481. https://doi.org/10.1016/j.conbuildmat.2017.12.121.

[15] J.T. San-José, I. Vegas, I. Arribas, I. Marcos, The performance of steel-making slag concretes in the hardened state, Mater. Des. 60 (2014) 612–619. https://doi.org/10.1016/J.MATDES.2014.04.030.

[16] A. Santamaría, V. Ortega-López, M. Skaf, J.A. Chica, J.M. Manso, The study of properties and behavior of self compacting concrete containing Electric Arc Furnace Slag (EAFS) as aggregate, Ain Shams Eng. J. 11 (2020) 231–243. https://doi.org/10.1016/j.asej.2019.10.001.

[17] J.A. Fuente-Alonso, V. Ortega-López, M. Skaf, Á. Aragón, J.T. San-José, Performance of fiber-reinforced EAF slag concrete for use in pavements, Constr. Build. Mater. 149 (2017) 629–638. https://doi.org/10.1016/j.conbuildmat.2017.05.174.

[18] A. Santamaría, A. Orbe, M.M. Losañez, M. Skaf, V. Ortega-Lopez, J.J. González, Self-compacting concrete incorporating electric arc-furnace steelmaking slag as aggregate, Mater. Des. 115 (2017) 179–193. https://doi.org/10.1016/J.MATDES.2016.11.048.

[19] L. Rondi, G. Bregoli, S. Sorlini, L. Cominoli, C. Collivignarelli, G. Plizzari, Concrete with EAF steel slag as aggregate: A comprehensive technical and environmental characterisation, Compos. Part B Eng. 90 (2016) 195–202. https://doi.org/10.1016/j.compositesb.2015.12.022.

[20] I. Sosa, C. Thomas, J.A. Polanco, J. Setién, P. Tamayo, High Performance Self-Compacting Concrete with Electric Arc Furnace Slag Aggregate and Cupola Slag Powder, Appl. Sci. 2020, Vol. 10, Page 773. 10 (2020) 773. https://doi.org/10.3390/APP10030773.

[21] L. Zongjin, Advanced concrete technology, John Wiley & Sons, Inc., 2011.

[22] V. Guerini, A. Conforti, G. Plizzari, S. Kawashima, Influence of Steel and Macro-Synthetic Fibers on Concrete Properties, Fibers. 6 (2018) 47. https://doi.org/10.3390/fib6030047.

[23] J.A.O. Barros, V.M.C.F. Cunha, A.F. Ribeiro, J.A.B. Antunes, Post-cracking behaviour of steel fiber reinforced concrete, Mater. Struct. 38 (2005) 47–56. https://doi.org/10.1617/14058.

[24] J. Torres, C. Andrade, J. Sánchez, I. Ciencias De La Construcción, E. Torroja, Periodo de iniciación de la corrosión por ión cloruro según la EHE 08 en elementos de hormigón fisurados, Inf. La Construcción. 72 (2020) e331–e331. https://doi.org/10.3989/IC.70275.

[25] Y. Zhan, G. Meschke, Multilevel Computational Model for Failure Analysis of Steel-Fiber–Reinforced Concrete Structures, J. Eng. Mech. 142 (2016) 04016090. https://doi.org/10.1061/(ASCE)EM.1943-7889.0001154.

[26] J. Barros, E. Pereira, A. Ribeiro, V. Cunha, J. Antunes, Self-compacting

steel fibre reinforced concrete for precasted sandwich panels – experimental and numerical research, Varenna, 2004.
[27] D.O. Al-Ghamdy, J.K. Wight, E. Tons, Flexural Toughness of Steel Fiber Reinforced Concrete, JKAU. 6 (1994) 81–97.
[28] N. Yousefieh, A. Joshaghani, E. Hajibandeh, M. Shekarchi, Influence of fibers on drying shrinkage in restrained concrete, Constr. Build. Mater. 148 (2017) 833–845. https://doi.org/10.1016/j.conbuildmat.2017.05.093.
[29] R. Gettu, D.R. Gardner, H. Saldivar, B.E. Barragfin, Study of the distribution :and orientation of fibers in SFRC specimens, Mater. Struct. (2004). https://doi.org/10.1617/14021.
[30] F. Laranjeira, C. Molins, A. Aguado, Predicting the pullout response of inclined hooked steel fibers, Cem. Concr. Res. 40 (2010) 1471–1487. https://doi.org/10.1016/j.cemconres.2010.05.005.
[31] L.G. Sorelli, A. Meda, G.A. Plizzari, Bending and Uniaxial Tensile Tests on Concrete Reinforced with Hybrid Steel Fibers, J. Mater. Civ. Eng. 17 (2005). https://doi.org/10.1061/(ASCE)0899-1561(2005)17:5(519).
[32] V. Ortega-López, A. Garcia-Llona, V. Revilla-Cuesta, A. Santamaría, J.T. San-José, Fiber-reinforcement and its effects on the mechanical properties of high-workability concretes manufactured with slag as aggregate and binder, J. Build. Eng. 43 (2021) 102548. https://doi.org/10.1016/j.jobe.2021.102548.
[33] A. Santamaría, A. García-Llona, V. Revilla-Cuesta, I. Piñero, V. Ortega-López, Bending tests on building beams containing electric arc furnace slag and alternative binders and manufactured with energy-saving placement techniques, Structures. 32 (2021) 1921–1933. https://doi.org/10.1016/j.istruc.2021.04.003.
[34] O.L. Manzoli, A.L. Gamino, E.A. Rodrigues, G.K.S. Claro, Modeling of interfaces in two-dimensional problems using solid finite elements with high aspect ratio, Comput. Struct. 94–95 (2012) 70–82. https://doi.org/10.1016/j.compstruc.2011.12.001.
[35] O.L. Manzoli, M.A. Maedo, L.A.G. Bitencourt, E.A. Rodrigues, On the use of finite elements with a high aspect ratio for modeling cracks in quasi-brittle materials, Eng. Fract. Mech. 153 (2016) 151–170. https://doi.org/10.1016/j.engfracmech.2015.12.026.
[36] O. Burgos-Montes, M. Palacios, P. Rivilla, F. Puertas, Compatibility between superplasticizer admixtures and cements with mineral additions, Constr. Build. Mater. 31 (2012) 300–309. https://doi.org/10.1016/j.conbuildmat.2011.12.092.
[37] J.J. Chen, A.K.H. Kwan, Y. Jiang, Adding limestone fines as cement paste replacement to reduce water permeability and sorptivity of concrete, Constr. Build. Mater. 56 (2014) 87–93. https://doi.org/10.1016/j.conbuildmat.2014.01.066.
[38] A.D./ D4792M-13(2019), Standard Test Method for Potential

Expansion of Aggregates from Hydration Reactions, 2019. https://doi.org/10.1520/D4792_D4792M-13R19.

[39] UNE 12390-3, Compressive strength of test specimens, 2014.

[40] UNE 12390-13, Determination of secant modulus of elasticity in compression, 2014.

[41] UNE 14651:2005+A1, Test method for metallic fibre concrete. Measuring the flexural tensile strength., 2008.

[42] S. Carmona, A. Aguado, New model for the indirect determination of the tensile stress-strain curve of concrete by means of the Brazilian test, Mater. Struct. 45 (2012) 1473–1485. https://doi.org/10.1617/s11527-012-9851-0.

[43] L. Ferrara, M. Di Prisco, Mode I fracture behavior in concrete: Nonlocal damage modeling, J. Eng. Mech. 127 (2001) 678–692. https://doi.org/10.1061/(ASCE)0733-9399(2001)127:7(678).

[44] G. Ruiz, M. Ortiz, A. Pandolfi, Three-dimensional finite-element simulation of the dynamic Brazilian tests on concrete cylinders, Int. J. Numer. Methods Eng. 48 (2000) 963–994. https://doi.org/10.1002/(SICI)1097-0207(20000710)48:7<963::AID-NME908>3.0.CO;2-X.

[45] K. Wille, S. El-Tawil, A.E. Naaman, Properties of strain hardening ultra high performance fiber reinforced concrete (UHP-FRC) under direct tensile loading, Cem. Concr. Compos. 48 (2014) 53–66. https://doi.org/10.1016/j.cemconcomp.2013.12.015.

[46] UNE 12390-6:2010, Tensile strength, 2014.

[47] J. Oliver, A. Huespe, M. Pulido, E. Chaves, From continuum mechanics to fracture mechanics: the strong discontinuity approach, Eng. Fract. Mech. 69 (2002) 113–136. https://doi.org/10.1016/S0013-7944(01)00060-1.

[48] F. Bencardino, L. Rizzuti, G. Spadea, R.N. Swamy, Stress-Strain Behavior of Steel Fiber-Reinforced Concrete in Compression, J. Mater. Civ. Eng. 20 (2008). https://doi.org/10.1061/(ASCE)0899-1561(2008)20:3(255).

[49] I. Yoshitake, W. Zhang, Y. Mimura, T. Saito, Uniaxial tensile strength and tensile Young's modulus of fly-ash concrete at early age, Constr. Build. Mater. 40 (2013) 514–521. https://doi.org/10.1016/j.conbuildmat.2012.11.022.

[50] D. Shen, X. Shi, S. Zhu, X. Duan, J. Zhang, Relationship between tensile Young's modulus and strength of fly ash high strength concrete at early age, Constr. Build. Mater. 123 (2016) 317–326. https://doi.org/10.1016/J.CONBUILDMAT.2016.06.145.

[51] B. Akcay, Experimental investigation on uniaxial tensile strength of hybrid fibre concrete, Compos. Part B Eng. 43 (2012) 766–778. https://doi.org/10.1016/J.COMPOSITESB.2011.08.017.

[52] J.G.. Van Mier, M.R.. Van Vliet, Influence of microstructure of concrete

on size/scale effects in tensile fracture, Eng. Fract. Mech. 70 (2003) 2281–2306. https://doi.org/10.1016/S0013-7944(02)00222-9.

[53] CEB-FIB, Model Code 2010 (Volume 1), 2012.

[54] A.C. 318, ACI Building Code Requirements for Reinforced Concrete (ACI 318-83), 1984.

[55] B.W. Xu, H.S. Shi, Correlations among mechanical properties of steel fiber reinforced concrete, Constr. Build. Mater. 23 (2009) 3468–3474. https://doi.org/10.1016/J.CONBUILDMAT.2009.08.017.

[56] A. Behnood, K.P. Verian, M. Modiri Gharehveran, Evaluation of the splitting tensile strength in plain and steel fiber-reinforced concrete based on the compressive strength, Constr. Build. Mater. 98 (2015) 519–529. https://doi.org/10.1016/j.conbuildmat.2015.08.124.

[57] A. Hillerborg, Results of three comparative test series for determining the fracture energy of concrete, Mater. Struct. 18 (1985) 407–413. https://doi.org/10.1007/BF02472416.

[58] B. Hwan Oh, D.G. Park, J.C. Kim, Y.C. Choi, Experimental and theoretical investigation on the postcracking inelastic behavior of synthetic fiber reinforced concrete beams, Cem. Concr. Res. 35 (2005) 384–392. https://doi.org/10.1016/J.CEMCONRES.2004.07.019.

[59] C. V.M.C.F., B. J.A.O., C. J.S., Pullout behaviour of hooked-end steel fibres in self-compacting concrete, 2007. https://doi:10.1061/(ASCE)MT.1943-5533.0000001.